Impact of Four-Wave-Mixing Noise from Dense Wavelength-Division-Multiplexing Systems on Entangled-State Continuous-Variable Quantum key Distribution

Shanna Du[1,2], Yan Tian,[1,2] and Yongmin Li[1,2,*]

[1]*State Key Laboratory of Quantum Optics and Quantum Optics Devices, Institute of Opto-Electronics, Shanxi University, Taiyuan 030006, China*

[2]*Collaborative Innovation Center of Extreme Optics, Shanxi University, Taiyuan 030006, China*

Integrating quantum key distribution (QKD) on the existing optical fiber network through dense wavelength-division multiplexing (DWDM) can greatly reduce the costs of quantum channels and improve the scalability and flexibility of the quantum communication network. In the scenarios of an access network or local area network with a large number of users, the connected optical fibers are relatively short and the quantum signal can be adjacent to the classical channels. In this case, the four-wave-mixing noise generated by the classical lights will have a severe impact on the performance of the QKD. We establish a theoretical model to characterize the excess noise in continuous-variable QKD induced by the four-wave mixing, and experimentally demonstrate the validity of the theoretical predictions. In addition, the influence of cross-phase-modulation noise between the carrier of the quantum signal and classical data channels on the QKD is investigated. To suppress the effect of the four-wave-mixing noise, an unequal channel spacing technique is employed. We realize coexistence of entangled state-based continuous-variable QKD and five adjacent DWDM classical channels with 10 dBm launch power and nonreturn-to-zero on-off-keying modulation at 2.5 Gb/s (10 Gb/s).

I. INTRODUCTION

Communication security plays a vital role in modern information society. Quantum key distribution (QKD) relies on the properties of quantum physics and has been demonstrated to be information-theoretically secure. In the past three decades, QKD has made great progress in both aspects of theoretical proof and experimental implementations [1–5]. Using optical fibers as the quantum channel, the QKD transmission distance has reached hundreds of kilometers recently. Note that most of the current quantum communication experimental systems are based on dedicated optical fibers. It is of great interest to deploy QKD on the existing optical fiber network by integrating it with the classical data channels through wavelength-division-multiplexing (WDM) technology. In this case, the costs of QKD can be reduced dramatically, and its scalability as well as flexibility can be improved. However, such coexistence of quantum communication and classical data is not straightforward, because the power of classical channels is much stronger than that of the quantum signal. When these vastly distinct signals are transmitted in the same optical fiber, excess noise photons are

inevitably introduced to the quantum signal and destroy the QKD's performance due to the imperfect isolation of the channels, the nonlinear effects of the optical fiber, and so on.

To address these challenges, a number of efforts have been made. In 1997, Townsend [6] adopted the coarse wavelength-division multiplexing (CWDM) (the spectral separation of the quantum and classical channels is over 200 nm) to reduce the effect of the excess noise on the discrete-variable quantum key distribution effectively. The feasibility of this approach has been further studied in several other works [7–11]. To reduce the quantum channel loss and increase the number of multiplexing classical channels, it is desired to place both the classical and quantum channels in the C-band using dense wavelength-division multiplexing (DWDM) with relatively narrow channel spacing (less than or equal to 1.6 nm). In this direction, several techniques have been developed to realize the coexistence of a large number of classical channels and quantum channels, considering the wideband response characteristics of conventional single photon detectors. These include reducing the launch power of the classical signals [12–15], adding narrow-band frequency-domain filters [12,13,15–18], and employing temporal filtering technology [12,14,17].

For continuous-variable quantum key distribution (CV QKD) [19] in which coherent detection is exploited, the involved local oscillator (LO) can act as a natural spectral filter without introducing additional losses, only the noise photons with the same spatiotemporal and polarization mode as the LO are effectively detected. In the past decade, the coexistence of CV QKD and classical light have attracted wide attentions since the pioneering work of Qi *et al.* [20]; these works demonstrated that the coherent state CV QKD exhibits good compatibility with the existing passive optical fiber network [21–25].

Most of the previous studies on the integration of QKD and WDM classical channels focus on the spontaneous Raman scattering (SRS) noise, which is regarded as the dominant noise source [20,21,23,25,26]. There are a few works [16] that investigate the effect of four-wave mixing (FWM) noises on the QKD and their contributions are usually neglected. This is enabled by locating the classical channels far away from the quantum channel [21,22], or delicately allocating the classical channels [13,23,27], in which case none of the FWM fields can fall into the quantum channel. On the other hand, some methods have been put forward to suppress the FWM, such as greatly reducing the classical optical power [13,28], increasing the channel spacing [16,21], and employing polarization multiplexing of classical and quantum signals [16]. Note that, for a long-distance optical fiber transmission (50 km or beyond), both the phase mismatch and the linear loss of the fiber strongly suppress the generated FWM noises.

In this work we consider the integration of CV QKD and classical data channels over access net work or the local area network in which (i) the fiber length is limited up to 20 km; (ii) both the quantum and classical channels are located at the C-band with 100 GHz channel spacing and the classical channels have standard launch power; (iii) there are no special allocations for the classical and quantum channels involved, which can be adjacent to each other. The last two scenarios ensure minimum alterations to the already deployed classical optical communication system as well as making full use of the channels (increasing the communication capacity). In this case, the FWM noises may become the dominant factor affecting the performance of CV QKD, and the involved mechanism is still obscure.

More precisely, we investigate the coexistence of entangled state-based CV QKD and five adjacent DWDM classical channels with 100 GHz channel spacing at the C-band over a single-mode fiber. The classical channels have a total launch power of 10 dBm and nonreturn-to-zero on-off-keying (NRZ OOK) modulation at 2.5 Gb/s or 10 Gb/s, respectively. We theoretically analyze the influence of FWM on the performance of CV QKD and investigate its correctness experimentally. The technique of unequal frequency spacing is proposed and demonstrated to eliminate the adverse impact of the FWM noises. Furthermore, we find that the cross-phase-modulation (XPM) may severely worsen the quantum communication besides the SRS and FWM noises when the classical data channels and QKD are copropagating, whereas such an effect is negligible when the quantum signal counterpropagates with classical data channels.

This paper is organized as follows. In Sec. II, we briefly discuss the influence of SRS noise on the quantum signal both in theory and experiment. In Sec. III, we present the theoretical model to analyze the FWM-induced channel excess noise in CV QKD, and characterize it experimentally. In Sec. IV, we measure and compare the quantum correlation of the entangled states versus fiber lengths under the condition of no classical light, forward classical light, or backward classical light. An effective approach is proposed to eliminate the effect of the FWM noise on CV QKD. Finally, we summarize our results and present an outlook in Sec. V.

II. SPONTANEOUS RAMAN SCATTERING NOISE

A. Experimental setup

As shown in Fig. 1, a multiplexer (MUX) and demultiplexer (DEMUX) with 100 GHz spacing, and two add-drop multiplexers (ADMs) are employed to multiplex and demultiplex the classical and quantum signals. There are three advantages of using ADM here. First, the insert loss added on the quantum channel is about 0.35 dB, which is less than that of a MUX or DEMUX (approximately 1 dB). Second, it can compensate the isolation degree of the MUX to the sideband photons of the classical channel at the quantum channel wavelength. For the classical light sources we use, the power of the sideband photons is approximately 46 dB below that of the carrier. The isolation degree of the MUX for the adjacent channel (nonadjacent channel) is 40 dB (80 dB), plus the ADM isolation of 27 dB, the sideband photons produced by the adjacent classical channel (nonadjacent channel) can be attenuated by 113 dB (153 dB) at the input port of the single-mode
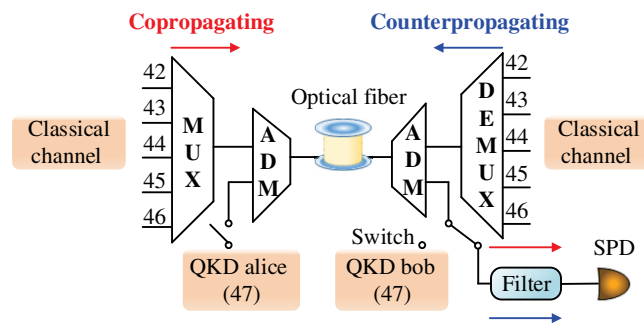

FIG. 1. Sketch of the forward and backward SRS measurement setup.

fiber, effectively eliminating the influence of sideband photons. Finally, the ADM improves the flexibility of adding and dropping the quantum signal.

At the DEMUX end, the classical channel lights can leak into the quantum channel due to the imperfect isolation of the ADM (40 dB for adjacent channels and 80 dB for nonadjacent channels). We add two optical filters with bandwidths of 0.57 nm and 80 dB isolation for adjacent channels to suppress the leakage of classical light before the single photon detector (SPD). By using the high-isolation optical filters, we can reduce the crosstalk noises from the classical channels to a negligible level, which is verified by observing that the measured back-to-back (no long-distance optical fiber) noise level is equal to the dark noise of the SPD in the presence of strong classical lights.

B. Analysis of SRS noise

For integration of QKD and DWDM classical channels, the crosstalk photons to the quantum channel generated by the carrier and sideband photons of strong classical optical signals can be greatly reduced using a high isolation degree MUX (DEMUX) and filters, as shown in Fig. 1. However, the inelastically scattered SRS with the same wavelength as that of the quantum channel is immune to such isolation. Considering a laser with power P_0 incident into an optical fiber with length L, and assuming that the average fiber loss coefficients of both the classical and quantum channels is α, the Raman noise per nanometer scattered on the quantum channel at the output port of the optical fiber can be written as [16]

$$
\begin{aligned}
P_{\text{ram,co}} &= P_0 \beta L e^{-\alpha L}, \\
P_{\text{ram,counter}} &= P_0 \frac{\beta}{2\alpha}(1 - e^{-2\alpha L}).
\end{aligned}
\tag{1}
$$

Here, β is the effective SRS coefficient with unit of $(\text{km nm})^{-1}$, $P_{\text{ram,co}}$ ($P_{\text{ram,counter}}$) is the generated forward (backward) SRS noise power on the quantum channel when the classical lights and quantum signal copropagate (counterpropagate) along the fiber of length L.

When a balanced homodyne detector (BHD) is utilized, the excess noise in shot noise units (SNU) contributed by SRS noise photons in the mode matching that of the LO is given by [20]

$$
\varepsilon_{\text{ram}} = 2\frac{\lambda^3}{hc^2}(\sigma P_{\text{ram}})\eta_B \eta_D,
\tag{2}
$$

where λ is the wavelength of the quantum signal, h is Planck's constant, c is the speed of light, P_{ram} represents $P_{\text{ram,co}}$ or $P_{\text{ram,counter}}$, σ represents the mode-matching efficiency between the SRS mode and the LO mode, and η_B and η_D represent the quantum efficiency of the BHD and the insertion loss of the DEMUX, respectively.

Note that SRS noise is much smaller than the shot noise when the incident single channel classical light power is weak. In order to reduce the influence of measurement uncertainties caused by the LO power fluctuations when the BHD is used to measure the Raman noise, we exploit the SPD to detect the Raman noise power and then use Eq. (2) to derive the excess noise. We also use the BHD to measure the SRS noises under the condition of relatively large Raman noises, and find that the measurement results are consistent with those of the SPD.

In Fig. 2(a) we show the forward SRS noises at 1539.77 nm (ITU channel 47) as a function of the single-mode fiber (G.652D) length at different total launch powers of the classical channels (ITU channels 42–46). It can be seen that the forward Raman power reaches the maximum at about a 20 km fiber length and then declines for longer distances due to the fiber attenuation. To measure the backward Ramon noises scattered on the quantum channel, we inject three (44–46 channels) counterpropagating classical
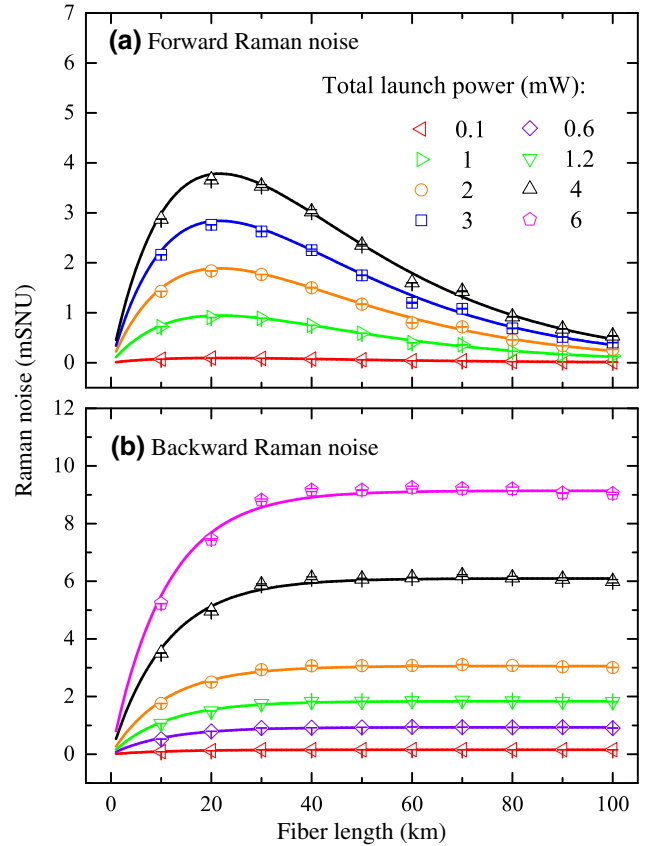

FIG. 2. Measured excess noises on ITU channel 47 versus the single-mode fiber length at the output port of the optical fiber. (a) The forward Raman noise. (b) The backward Raman noise. The total power of the classical channels (ITU channels 42–46) varies from 0.1 to 6 mW. Theoretical fittings (solid line) are plotted using Eqs. (1) and (2) with Raman coefficients $\beta_{\text{forward}} = 1.934 \times 10^{-9}$ $(\text{km nm})^{-1}$ and $\beta_{\text{backward}} = 2.307 \times 10^{-9}$ $(\text{km nm})^{-1}$.

lights into the optical fiber simultaneously. In Fig. 2(b) we depict the dependence of the backward SRS noise versus the fiber length at total launch powers of 0.1, 0.6, 1.2, 2, 4, and 6 mW. The behavior of the backward Raman noise is obviously different from that of the forward Raman noise. The former increases quickly when the fiber length is less than 30 km and then gradually reaches saturation. In terms of the measurement results, the Raman coefficient is determined within a range of $1.9 \times 10^{-9} \sim 2.5 \times 10^{-9}$ (km nm)$^{-1}$, which depends on the concrete wavelength of the five classical channels.

To reduce the influence of the SRS, the quantum channel can be placed at the bottom of the SRS spectrum close to the original laser [13] where the noise level is relatively low. Furthermore, the quantum channel can be set to be blue detuned to the classical channels, due to the fact that anti-Stokes noise is weaker than Stokes noise.

III. FOUR-WAVE-MIXING NOISE

A. FWM in optical fiber

When the light field propagates in an optical fiber, in the case in which a slowly varying envelope approximation and only the FWM effect is considered, that is, neglecting the Raman process and phase modulation process, the nonlinear Schrödinger equation describing the generated idler field in the frequency domain is given by [29]

$$
\frac{\partial A_i(z, \Omega_i)}{\partial z} = \left[ik(\Omega_i) - \frac{\alpha}{2} \right] A_i(z, \Omega_i) + i\gamma Dp \frac{\hbar \omega_0}{(2\pi)^2}
$$
$$
\times \iint d\Omega_s \, d\Omega_l A_s(z, \Omega_s)^* A_l(z, \Omega_l) A_h(z, \Omega_h),
$$
(3)

where $A_s(z, \Omega_s)$, $A_l(z, \Omega_l)$, and $A_h(z, \Omega_h)$ represent the signal field and the two pump fields, $A_i(z, \Omega_i)$ is the generated idler field, z is the transmission distance of the interacting light fields in the optical fiber, $\Omega_{i(s,l,h)}$ is the frequency shift of each optical field relative to its carrier frequency $\omega_{i0(s0,l0,h0)}$, k is the propagation wave vector, γ is the third-order nonlinear coefficient of the fiber, α is the fiber loss factor, D is the degenerate factor ($D = 1$ or 2 for the case of degeneracy or nondegeneracy), p is the polarization factor ($p = 1$ or $1/3$ for the case of identical polarization or orthogonal polarization of the signal and pump fields), $\hbar \omega_0$ is the single photon energy, and ω_0 is the carrier frequency.

As we consider only the average field and neglect the fluctuations part, we obtain

$$
A_s(z, \Omega_s)^* = 2\pi A_s(0, \omega_{s0})^* e^{(-ik_{s0} - \alpha/2)z} \delta(\Omega_s), \quad (4)
$$

$$
A_l(z, \Omega_l) = 2\pi A_l(0, \omega_{l0}) e^{(ik_{l0} - \alpha/2)z} \delta(\Omega_l), \quad (5)
$$

$$
A_h(z, \Omega_h) = 2\pi A_h(0, \omega_{h0}) e^{(ik_{h0} - \alpha/2)z} \delta(\Omega_h). \quad (6)
$$

Substituting Eqs. (4)–(6) into (3), and using the initial condition that the idler field is in a vacuum state at $z = 0$, we obtain the solution of the idler field as

$$
A_i(z, \Omega_i) = i\gamma Dp \hbar \omega_0 \, e^{[ik(\Omega_i) - \alpha/2]z} \frac{e^{(i\Delta k_0 - \alpha)z} - 1}{i\Delta k_0 - \alpha}
$$
$$
\times 2\pi A^*(0, \omega_{s0}) A(0, \omega_{h0}) A(0, \omega_{l0}) \delta(\Omega_i), \quad (7)
$$

where $\Delta k_0 = k_{h0} + k_{l0} - k_{s0} - k_{i0}$ and $k(\Omega_i)$ is the wave vector of the idler field with frequency shift Ω_i relative to its carrier frequency.

Using Eq. (7), the average power of the FWM field takes the form [30]

$$
P_i(z, \Delta k) = \gamma^2 D^2 p^2 \, e^{-\alpha z} \left| \frac{1 - e^{(i\Delta k - \alpha)z}}{i\Delta k - \alpha} \right|^2 P_s P_l P_h
$$
$$
= \eta \gamma^2 D^2 p^2 \, e^{-\alpha z} \frac{(1 - e^{-\alpha z})^2}{\alpha^2} P_s P_l P_h, \quad (8)
$$

where the coefficients are given by

$$
\eta = \frac{\alpha^2}{\alpha^2 + \Delta k^2} \left[1 + \frac{4e^{-\alpha z} \sin^2(\Delta kz/2)}{(1 - e^{-\alpha z})^2} \right], \quad (9)
$$

$$
\Delta k = \frac{2\pi \lambda_s^2}{c} |f_l - f_s| |f_h - f_s| D_c(\lambda_s). \quad (10)
$$

Here, η is the phase matching efficiency for FWM, $f_{s(l,h)}$ and $P_{s(l,h)}$ are the optical frequency and power of signal and pump fields, respectively. $\alpha = (\ln 10/10) \, a$ represents the loss coefficient and a is the fiber attenuation rate in unit of dB per km. $D_c = (s/4)(\lambda_s - \lambda_0^4/\lambda_s^3)$ is the dispersion coefficient of optical fiber. For the single-mode fiber (G.652D) we used, which has a zero dispersion slope s of 0.08, zero dispersion wavelength λ_0 of 1313 nm, and third-order nonlinear coefficient of $\gamma = 1.441/(\text{W km})$.

B. Excess noises induced by FWM

In this part, we analyze and calculate the added excess noise in a CV QKD system arising from the FWM field generated by the pulse-modulated classical light fields. Assume that the generated FWM field is detected by a BHD at receiver Bob's site, and that the frequency difference between the FWM field (ω_i) and the LO (ω_L) is $\Delta\Omega = \omega_i - \omega_L$ with a relative phase between the LO and the FWM fields of θ (hereafter we assume that θ follows a uniform distribution on $[0, 2\pi]$ because the FWM and LO fields are independent of each other). In this case, the

output photocurrent of the BHD that is proportional to the quadrature of the modulated FWM light field has the form

$$\hat{i}_- \propto \hat{X}'_{i,\theta}(t, \Delta\Omega) = \hat{X}_{i,\theta}(t, \Delta\Omega)\phi(t) + \hat{X}_V(t, \Delta\Omega)\phi'(t),$$
(11)

where $\hat{X}_{i,\theta}(t, \Delta\Omega)$ is the quadrature of the FWM field generated by the continuous-wave classical light fields

$$\hat{X}_{i,\theta}(t, \Delta\Omega) = \hat{A}_i \, e^{-i(\Delta\Omega t + \theta)} + \hat{A}_i^\dagger \, e^{i(\Delta\Omega t + \theta)},$$
(12)

$\hat{X}_V(t, \Delta\Omega)$ represents the quadrature of the vacuum field, $\phi(t)$ represents the pulse wave pattern of the FWM field, and $\phi'(t) = 1 - \phi(t)$ is the complementary waveform of $\phi(t)$. We assume that the NRZ OOK modulation format that is widely employed in metro networks is used for the classical data channels

$$\phi(t) = \sum_{k=-\infty}^{+\infty} b_k P(t - kT_p),$$
(13)

$$\phi'(t) = \sum_{k=-\infty}^{+\infty} (1 - b_k) P(t - kT_p),$$
(14)

where $P(t)$ denotes the pulse shape, T_p denotes the interval time of data bits, and b_k denotes the binary random number (0 or 1).

In the CV QKD system, the pulse width of the pulsed quantum signal field is assumed to be T_0. By integrating

$\hat{X}'_{i,\theta}(t, \Delta\Omega)$ from $-T_0/2$ to $T_0/2$, we obtain the quadrature of the pulsed quantum signal state

$$\hat{X}''_{i,\theta} = \frac{1}{\sqrt{T_0}} \int_{-T_0/2}^{T_0/2} \hat{X}'_{i,\theta}(t, \Delta\Omega) \, dt$$

$$= \frac{\sqrt{T_0}}{2\pi} \int_{-\infty}^{+\infty} \hat{X}'_{i,\theta}(\omega) \, \text{sinc}(\omega T_0/2) \, d\omega$$
(15)

and its variance

$$\langle (\Delta\hat{X}''_{i,\theta})^2 \rangle = \frac{T_0}{(2\pi)^2} \iint_{-\infty}^{+\infty} \langle \hat{X}'_{i,\theta}(\omega)\hat{X}'_{i,\theta}(\omega') \rangle$$

$$\times \text{sinc}(\omega T_0/2) \, \text{sinc}(\omega' T_0/2) \, d\omega \, d\omega', \quad (16)$$

where $\hat{X}'_{i,\theta}(\omega)$ is obtained via the Fourier transform of $\hat{X}'_{i,\theta}(t, \Delta\Omega)$:

$$\hat{X}'_{i,\theta}(\omega) = \frac{1}{2\pi} \left[\int_{-\infty}^{+\infty} \phi(\omega_1)\hat{X}_{i,\theta}(\omega - \omega_1) \, d\omega_1 \right.$$

$$\left. + \int_{-\infty}^{+\infty} \phi'(\omega_1)\hat{X}_V(\omega - \omega_1) \, d\omega_1 \right], \quad (17)$$

$$\hat{X}'_{i,\theta}(\omega') = \frac{1}{2\pi} \left[\int_{-\infty}^{+\infty} \phi(\omega_2)\hat{X}_{i,\theta}(\omega' - \omega_2) \, d\omega_2 \right.$$

$$\left. + \int_{-\infty}^{+\infty} \phi'(\omega_2)\hat{X}_V(\omega' - \omega_2) \, d\omega_2 \right]. \quad (18)$$

Substituting Eqs. (17) and (18) into Eq. (16), we obtain

$$\langle (\Delta\hat{X}''_{i,\theta})^2 \rangle = \frac{T_0}{(2\pi)^4} \iiiint_{-\infty}^{+\infty} [\langle \phi(\omega_1)\phi(\omega_2) \rangle \langle \hat{X}_{i,\theta}(\omega - \omega_1)\hat{X}_{i,\theta}(\omega' - \omega_2) \rangle + \langle \phi'(\omega_1)\phi'(\omega_2) \rangle \langle \hat{X}_V(\omega - \omega_1)\hat{X}_V(\omega' - \omega_2) \rangle]$$

$$\times \text{sinc}(\omega T_0/2) \, \text{sinc}(\omega' T_0/2) \, d\omega_1 \, d\omega_2 \, d\omega \, d\omega'.$$
(19)

Because we only care about the FWM-induced excess noise that is connected with the first term on the right-hand side of Eq. (19), the second term (vacuum fluctuation) is dropped hereafter.

Using Eq. (13), $\langle \phi(\omega_1)\phi(\omega_2) \rangle$ can be expressed as

$$\langle \phi(\omega_1)\phi(\omega_2) \rangle = \iint_{-\infty}^{\infty} \langle \phi(t_1)\phi(t_2) \rangle e^{i\omega_1 t_1} e^{i\omega_2 t_2} \, dt_1 \, dt_2$$

$$= 2\pi \delta(\omega_1 + \omega_2) \int_{-\infty}^{+\infty} R_0(\tau) e^{i\omega_1 \tau} \, d\tau$$

$$+ \int_{-2T}^{2T} d\tau \, e^{i\omega_1 \tau} \sum_{n=1}^{\infty} R_1(\tau, n)$$

$$\times \left[\delta\left(\omega_1 + \omega_2 - \frac{2n\pi}{T_p} \right) \right.$$

$$\left. + \delta\left(\omega_1 + \omega_2 + \frac{2n\pi}{T_p} \right) \right], \quad (20)$$

where $\tau = t_1 - t_2$. In order to simplify the theoretical analysis, we assume that the pulsed classical fields share the same synchronous clock but with independent pulse modulation sequences. There are two different types of FWM

process, the first is the degenerate FWM process in which only a single pump field is launched. In this case, $R_0(\tau)$ and $R_1(\tau, n)$ are written as

$$R_0(\tau) = \frac{1}{T_p} \int_{-T_p/2}^{T_p/2} \langle \phi(t_1)\phi(t_2) \rangle \, dt_1$$

$$= \begin{cases} \dfrac{3}{16}\left(1 - \dfrac{|\tau|}{T_p}\right) + \dfrac{1}{16} & \text{if } |\tau| \leq T_p, \\ \dfrac{1}{16} & \text{if } |\tau| > T_p, \end{cases} \quad (21)$$

$$R_1(\tau, n) = \frac{3\pi}{8}\left(1 - \frac{|\tau|}{T_p}\right) \text{sinc}\left[n\pi\left(1 - \frac{|\tau|}{T_p}\right)\right]. \quad (22)$$

The second scenario is the nondegenerate FWM in which two pump fields are involved with different frequencies and pulse modulation sequences. The resulting $R_0(\tau)$ and $R_1(\tau, n)$ are given by

$$R_0(\tau) = \begin{cases} \dfrac{7}{64}\left(1 - \dfrac{|\tau|}{T_p}\right) + \dfrac{1}{64} & \text{if } |\tau| \leq T_p, \\ \dfrac{1}{64} & \text{if } |\tau| > T_p, \end{cases} \quad (23)$$

$$R_1(\tau, n) = \frac{7\pi}{32}\left(1 - \frac{|\tau|}{T_p}\right) \text{sinc}\left[n\pi\left(1 - \frac{|\tau|}{T_p}\right)\right]. \quad (24)$$

If all of the interacting signal and pump fields have the same clock and pulse modulation sequence, the corresponding correlation function can be written as

$$R_0(\tau) = \begin{cases} \dfrac{1}{4}\left(1 - \dfrac{|\tau|}{T_p}\right) + \dfrac{1}{4} & \text{if } |\tau| \leq T_p, \\ \dfrac{1}{4} & \text{if } |\tau| > T_p, \end{cases} \quad (25)$$

$$R_1(\tau, n) = \frac{\pi}{2}\left(1 - \frac{|\tau|}{T_p}\right) \text{sinc}\left[n\pi\left(1 - \frac{|\tau|}{T_p}\right)\right]. \quad (26)$$

By substituting Eqs. (25) and (26) into Eq. (20), we obtain

$$\langle \phi(\omega_1)\phi(\omega_2) \rangle = \pi^2 \delta(\omega_1 + \omega_2)\delta(\omega_1)$$
$$+ \frac{\pi}{2}\delta(\omega_1 + \omega_2)T_p \, \text{sinc}^2\left(\frac{T_p\omega_1}{2}\right) + \Delta, \quad (27)$$

where

$$\Delta = \sum_{n=1}^{\infty} R_1(\omega_1, n)\left[\delta\left(\omega_1 + \omega_2 - \frac{2n\pi}{T_p}\right) \right.$$
$$\left. + \delta\left(\omega_1 + \omega_2 + \frac{2n\pi}{T_p}\right)\right].$$

We define the Fourier transform of $\hat{X}_{i,\theta}(t, \Delta\Omega)$ as $\hat{X}_{i,\theta}(\omega)$, which has the form

$$\hat{X}_{i,\theta}(\omega) = \hat{A}_i(z, \omega - \Delta\Omega)\, e^{-i\theta} + \hat{A}_i(z, -\omega - \Delta\Omega)^\dagger \, e^{i\theta}. \quad (28)$$

From Eq. (7), we have

$$\hat{A}_i(z, \omega) = i\gamma Dp\hbar\omega_0\, e^{[ik(\omega)-\alpha/2]z}\frac{e^{(i\Delta k-\alpha)z} - 1}{i\Delta k - \alpha}A_s^*(0, \omega_{so})$$
$$\times A_l(0, \omega_{lo})A_h(0, \omega_{ho})2\pi\delta(\omega)$$
$$= \bar{A}_i(z, \omega)2\pi\delta(\omega). \quad (29)$$

By substituting Eqs. (27), (28), and (29) into Eq. (19), and considering that θ follows a uniform distribution on $[0, 2\pi]$, we obtain

$$\langle (\Delta\hat{X}_i'')^2 \rangle = \frac{T_0}{(2\pi)^2}|\bar{A}_i(z, 0)|^2$$

$$\times \int_{-\infty}^{+\infty}\int_{-\infty}^{+\infty}\left[\pi^2\delta(\omega_1 + \omega_2)\delta(\omega_1)\right.$$

$$+ \frac{\pi}{2}\delta(\omega_1 + \omega_2)T_p\text{sinc}^2\left(\frac{T_p\omega_1}{2}\right) + \Delta\bigg]$$

$$\times \left\{\text{sinc}\left[\frac{(\omega_1 + \Delta\Omega)T_0}{2}\right]\text{sinc}\left[\frac{(\omega_2 - \Delta\Omega)T_0}{2}\right]\right.$$

$$\left. + \text{sinc}\left[\frac{(\omega_1 - \Delta\Omega)T_0}{2}\right]\text{sinc}\left[\frac{(\omega_2 + \Delta\Omega)T_0}{2}\right]\right\}d\omega_1 d\omega_2. \quad (30)$$

Under current conditions, the repetition rates of the classical data (the order of 10 GHz) are much higher than that (several tens of megahertz) of the CV QKD; therefore, we have $T_0 \gg T_p$. In this case, by integrating with respect to ω_1 and ω_2, Eq. (30) is reduced to

$$\langle (\Delta \hat{X}_i'')^2 \rangle = \frac{T_0}{2} |\bar{A}_i(z,0)|^2 \mathrm{sinc}^2 \left(\frac{\Delta \Omega T_0}{2} \right) + \frac{T_p}{2} |\bar{A}_i(z,0)|^2. \tag{31}$$

Under the condition that $\Delta \Omega T_0 \gg 1$, which is usually satisfied in a real scenario, the first term on the right-hand side of Eq. (31) is approximately zero. Therefore, when all the classical fields involved in the FWM process have synchronous clocks and the same pulse modulation sequences, the excess noise produced by the FWM field is of the form

$$\langle (\Delta \hat{X}_i'')^2 \rangle = \frac{T_p}{2} |\bar{A}_i(z,0)|^2, \tag{32}$$

where $|\bar{A}_i(z,0)|^2$ is the average photon number of the continuous-wave FWM field.

In a similar way, by substituting Eqs. (21)–(24) into Eq. (20), we obtain the excess noise generated by the degenerate FWM

$$\langle (\Delta \hat{X}_i'')^2 \rangle = \frac{3 T_p}{8} |\bar{A}_i(z,0)|^2 \tag{33}$$

and the excess noise generated by the nondegenerate FWM process

$$\langle (\Delta \hat{X}_i'')^2 \rangle = \frac{7 T_p}{32} |\bar{A}_i(z,0)|^2. \tag{34}$$

From the results of Eqs. (32), (33), and (34), we find that the FWM-induced excess noise mainly depends on the average photon number of the continuous-wave FWM field $|\bar{A}_i(z,0)|^2$ and the interval time of the classical data bit T_p.

C. Measurement of the photon number of FWM

In this section we measure the average photon number of the continuous-wave FWM field using the SPD (Fig. 1). We consider the worst case, where the classical light fields have the same polarization. In Fig. 3 we show the detected SRS and FWM noise powers in the quantum channel (ITU channel 47) versus the fiber length. Five adjacent classical channels, each with a power of 2 mW, are located at ITU channel 42 to channel 46 (100 GHz channel interval). They are all linearly polarized along the same direction by using manual polarization controllers. It is obvious that FWM dominates the total noise power at a relatively short fiber length of less than 20 km. With the increasing fiber length, the FWM noise decreases quickly and reaches a level comparable to that of SRS when the length of the fiber approaches 50 km.
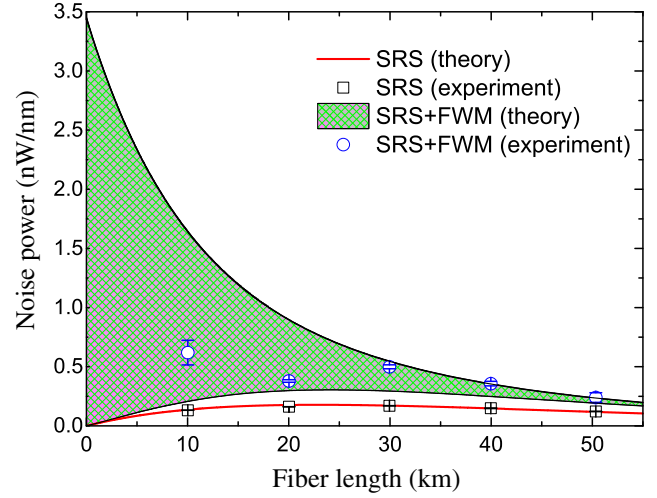

FIG. 3. SRS and FWM noise powers on the quantum channel (ITU 47 channel) versus the fiber length. The five adjacent classical channels are located at ITU 42–46 (100 GHz channel interval). The red curve and shaded area represent the theoretical fittings of SRS noises and total SRS and FWM noises, respectively, while the black squares and blue circles are the corresponding experimental results.

There are six different combinations for the classical channels to generate the FWM fields on the quantum channel, including two cases of the degenerate FWM process ($\lambda_l = \lambda_h$) where $D = 1$, and four cases of the nondegenerate FWM process ($\lambda_l \neq \lambda_h$) where $D = 2$. For each combination, it can be seen from Eqs. (9) and (10) that the phase matching efficiency η of FWM will oscillate periodically along with the fiber length. The period of the six combinations varies from 140 to 830 m. To predict the theoretical FWM power versus the fiber length, we sum the six FWM powers at each fiber length. However, the efficiency of FWM η is very sensitive to the frequencies of the interacting classical lights as well as the fiber length; more precisely, a frequency shift of several hundred megahertz or a fiber length variation of several hundred meters can result in significant variations of η. Therefore, to reasonably reflect all possible FWM powers, the envelope of the maximum (minimum) values of the FWM power for each combination is extracted and then summed. In this way, we obtain the theoretical upper (lower) bound and the corresponding distribution range of the FWM noise power versus the length of the single-mode fiber, as shown by the shaded area in Fig. 3.

D. Measurement of the excess noise arising from FWM

In this section we use the BHD to characterize the excess noises caused by the FWM when pulse-modulated classical data channels coexist with the quantum channel. Five classical channels (ITU channels 42–46; Fig. 4) are modulated by the NRZ OOK format at 2.5 Gb/s (10 Gb/s) using
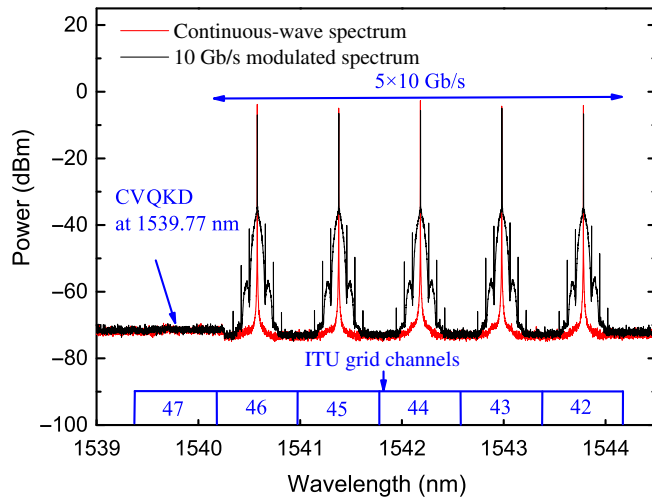
FIG. 4. The spectrum of the DWDM classical channels. The red lines represent the spectrum in the case of the continuous wave, while the black lines are the spectrum of the modulated lights at 10 Gb/s PRBS. The QKD channel is also marked.

$2^{23} - 1$ bit pseudorandom binary sequences (PRBSs). In comparison with the optical spectrum without modulation, the modulated spectrum with 10 Gb/s is broadened with symmetrical small peaks at 0.08 nm (10 GHz) and its harmonics. In Fig. 5 we depict the recorded PRBS waveforms and eye diagrams of the modulated classical light with 2 mW of single channel power and through a 50 km single-mode optical fiber transmission. The large vertical eye opening indicates a high signal-to-noise ratio and low bit error rates of the classical communication.

As shown in Fig. 6, we disconnect the CV QKD setup at both Alice's and Bob's sides, and measure the excess noise generated on the quantum channel at the receiver Bob after the modulated classical lights propagate through different lengths of fibers. To consider the worst case, polarization controllers (PCs) and a polarization beam splitter (PBS) are utilized to make the five classical lights have identical linear polarization states. An arbitrary waveform generator (AWG) generates $2^{23} - 1$ PRBS electrical pulse signals, which drive an amplitude modulator (AM) to modulate the five continuous classical lights. The modulated classical lights then transmit through different lengths of single-mode fibers. At the receiver side, the generated excess noise on the quantum channel is measured by a 1.6 GHz bandwidth BHD, in which a single frequency laser at 1539.77 nm with linewidth of 5 kHz acts as the LO. Before the BHD, an isolator and a polarizer are inserted. The former is used to suppress the fluctuation of the shot noise caused by the reflection of the LO, and the latter is employed to ensure the polarization of the noise photons matching that of the LO and can be fully detected by the BHD. After the in-line polarizer, an SPD is used to measure the average photon number of the noise photons.
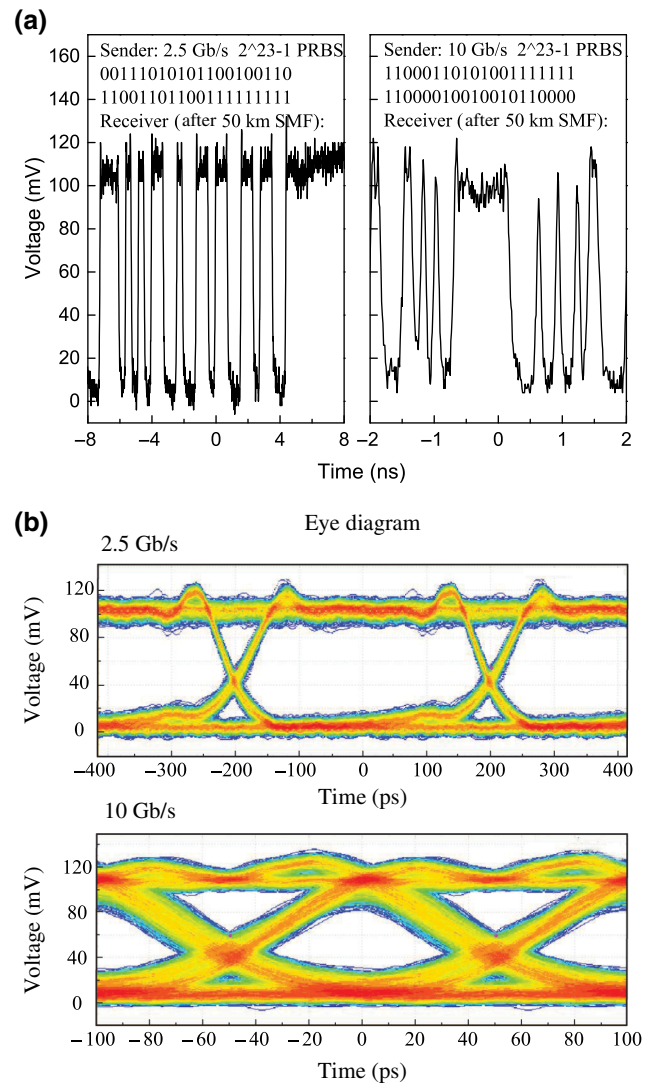

FIG. 5. PRBS waveform (a) and eye diagram (b) of the modulated classical light with 2 mW of single channel power after a 50 km single-mode fiber transmission. The modulation speeds are 2.5 and 10 Gb/s, respectively.

In Fig. 7 we illustrate the measured FWM and SRS noises on the quantum channel (ITU channel 47 or 47.5) versus the length of the single-mode fiber. The inset shows the allocation of various channels. The QKD pulsed signal has a repetition rate of 50 kHz and pulse width of 10 μs. The field quadratures of the SRS and FWM are detected by the BHD with a signal-to-noise ratio of 14 dB and quantum efficiency of $\eta_B = 0.8$. Its output voltage signals are acquired by a data acquisition card with a sampling rate of 10 MHz/s. The recorded data (200 M data for each cycle) are mixed with a 3.5 MHz sine signal and low-pass filtered through a 0.5 MHz low-pass filter. The resulting signals are then integrated within the pulse width (from 0 to T_0) to obtain the field quadrature (1 M data) for the pulsed quantum states, from which the variance of the field
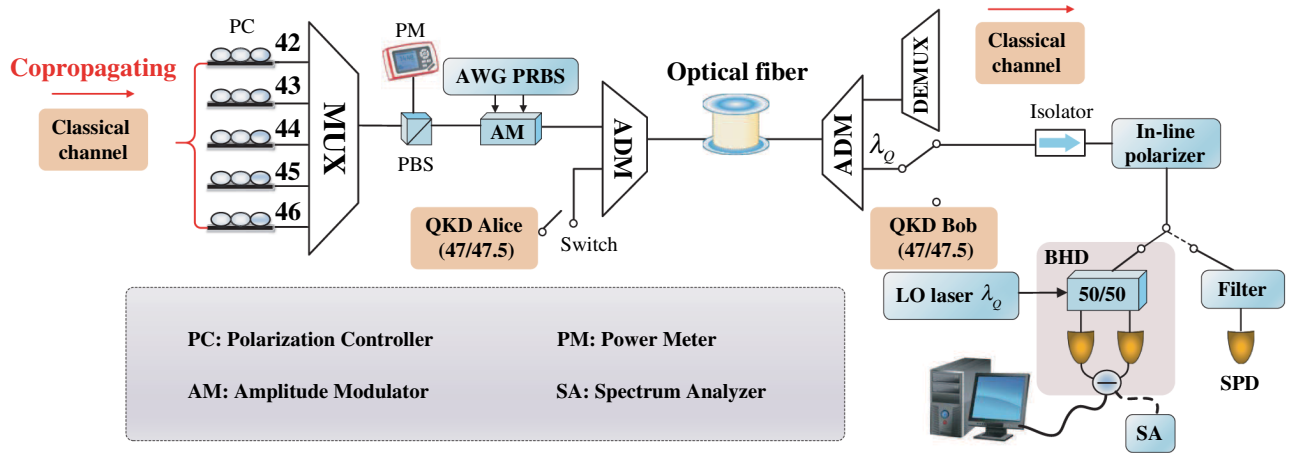
FIG. 6. Measurement of the excess noises caused by the FWM and SRS. The quantum channel coexists with five adjacent modulated classical channels with a 100 GHz channel interval.

quadrature V_m is derived. The noise variance at the single-mode fiber output $V(x_{in})$ is inferred based on the beam splitter model with $V(x_{in}) = (V_m - 1)/(\eta_B \eta_D) + 1$, where $\eta_D = 0.75$ denotes the propagation loss from the output port of the single-mode fiber to the BHD.

The observed SRS and FWM noises on channel 47 decrease with the fiber length despite the different modulation frequencies. Given the fiber length, the noise under a modulation of 2.5 Gb/s is significantly higher than that under a modulation of 10 Gb/s. This phenomenon is consistent with the prediction of Eqs. (31)–(34), and attributed to the fact that a lower modulation bandwidth leads to a higher noise power density spectrum at the QKD signal band for the same continuous FWM power. The total excess noise mainly includes FWM noise and SRS noise, in which FWM takes the majority, while SRS accounts for only a small part with value less than 10 mSNU.

To suppress the FWM noise that is detrimental to the QKD, we make use of the unequal channel spacing technique and move the quantum channel from 47 to 47.5. In this case, the noises observed at 1539.37 nm (ITU channel 47.5) are dramatically smaller than those observed at ITU channel 47, because any FWM component generated from the equal spacing DWDM channels does not overlap with the QKD channel, which lies in the middle of two adjacent DWDM channels. More precisely, five classical channels located on channels 42–46 at the identical spacing (100 GHz) generate FWM fields that are also located on the same 100 GHz grid, such as channels 47 and 48, due to the energy conservation of FWM. These FWM noises center on the channel's central wavelength and are very weak at the boundaries between the channels.

To determine the theoretical value of the excess noises, the photon number of the SRS induced by each classical channel is measured by the SPD and the total SRS photon number is obtained. Next, we measure the noise photon number under the coexistence of all five channels, and the average photon number of FWM is obtained by subtracting the total SRS photon number. The resulting SRS and FWM photon numbers are divided by the total loss from the fiber output to the detector (including the detector's efficiency) to infer the photon number at the fiber output. These values are then respectively substituted into Eqs. (2) and (32) to calculate the corresponding excess noise. By summing the SRS and FWM excess noises, the theoretical value of the total excess noise is derived.

The mode-matching efficiency σ between the SRS mode and LO mode in Eq. (2) is derived as follows. We consider the worst scenario, i.e., the measured excess noises are maximized by controlling the polarization controller in front of the isolator. In this case, we measure the ratio between the noise photon number after and before the in-line polarizer. It is observed that the ratio lies between 0.58 and 0.66 for the SRS noise, which is exactly the value of σ in Eq. (2). Similarly, we also measure the corresponding ratio for the FWM noise and find its value is in the range of about 0.6 to 0.8.

IV. COEXISTENCE OF AN ENTANGLED STATE CV QKD AND INTENSE DWDM DATA CHANNELS

As show in Fig. 6, we connect the entangled state based CV QKD system [31] with the ADM at both Alice's and Bob's sides, where the wavelength of the QKD quantum signal is set to 1539.37 nm to suppress the FWM noise. The directly measured two-mode squeezing and antisqueezing levels of the Einstein-Podolsky-Rosen (EPR) state at Alice's site are 5.5 and 11.6 dB, respectively. Under the coexistence of QKD and classical light transmission, the field quadrature correlation of the EPR states distributed to Alice and Bob versus the fiber length are shown in Fig. 8. The correlation coefficient is defined as

$\rho_{AB} = \text{Cov}(A, B)/\sqrt{\text{Var}(A)\,\text{Var}(B)}$, where $\text{Cov}(A, B)$ is the covariance between Alice's and Bob's measured quadrature data, and $\text{Var}(A)$ [$\text{Var}(B)$] is the variance of Alice (Bob). We can see that the observed quadrature correlations (the pink diamonds and purple triangles) decrease with the fiber length in the case of a copropagating QKD signal and classical channels. The correlations are much lower than those of the theoretical predictions (black squares).

The degradation of the correlation is attributed to the cross-phase-modulation noise between the carrier of the QKD quantum signal and the classical channels; the XPM noise interferes with the QKD and seriously destroys its performance. Specially, the pulsed classical lights modulate the phase and amplitude of the carrier wave of the quantum signal in a quasicontinuous wide spectrum manner (Fig. 4), which covers the frequency range of the quantum signal. The random modulation scatters a small portion of the carrier of the quantum signal to its sideband and adds noise photons to the received quantum signal of Bob, which deteriorates the observed correlations between Alice and Bob. To verify the existence of the XPM, we reduce the carrier power of the quantum signal; it is found that the quadrature correlation degree increases obviously. On the other hand, if we switch off the modulation of the classical light and launch the continuous classical light into the single fiber, the quadrature correlation will also increase significantly, which is very close to the values of no classical light input.

It is worth noting that the influence of the XPM noise mainly occurs in the situation of copropagation of the quantum signal and classical light. For the counterpropagation case, the quantum signal and classical light are not synchronized; the resulting average XPM effect on the quantum signal is extremely small. This conjecture is confirmed in our experiment; in the case of counterpropagation of the QKD and classical light, the correlation degree between Alice and Bob is restored and almost overlapped with the case of no classical light input. The insets in Fig. 8 illustrate typical quadrature correlation outcomes of the amplitude quadratures of the EPR states after 30 km of fiber transmission. The black and blue points denote the shot noise data and quadrature data of Alice and Bob, respectively, which are normalized to the noise standard deviation of a vacuum state. From the data, we can derive the conditional variance $V_{A|B}$, which has a value of 0.957 and 12.25 for the counterpropagation and copropagation, respectively. This indicates that the EPR entanglement is broken for the copropagation, but retained for the counterpropagation.

To investigate the security performance of our entanglement-based QKD system when classical data channels exist, we utilize the approach of Ref. [31] and the references therein. The experimental parameters required for estimating the secret key rate include the covariance matrices of Alice's and Bob's modes, the parameters of Alice's (Bob's) BHD with electronic noise $\upsilon_{A,\text{el}} = 0.005$
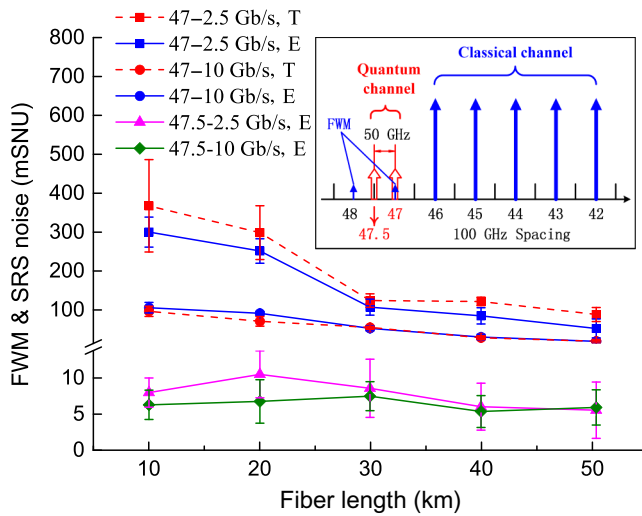

FIG. 7. FWM and SRS noises on ITU channels 47 (1539.77 nm) and 47.5 (1539.37 nm) versus the length of a single-mode fiber. The inset shows the placement of various channels. Five classical channels (ITU channels 42–46) with a total power of 10 dBm are modulated at 2.5 Gb/s or 10 Gb/s and are able to generate FWM noise located on channels 47 and 48. We use an E to denote experimental results using the BHD, and a T to denote theoretical values calculated by substituting the measured average photon number into Eqs. (2) and (32).
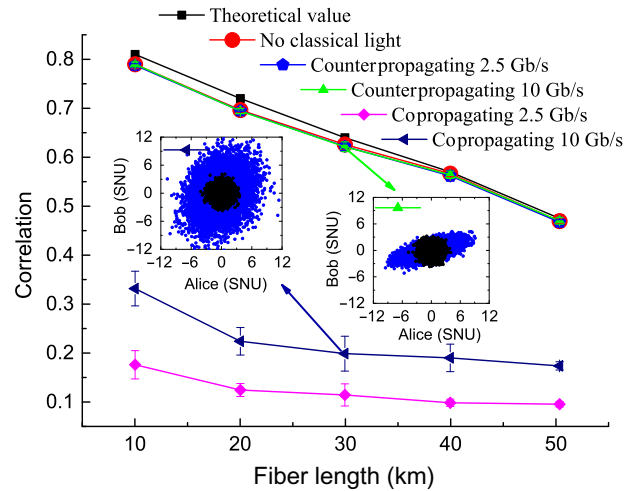

FIG. 8. Observed correlation between Alice's and Bob's data when the entangled state CV QKD coexists with five DWDM classical channels. The insets show the correlation between Alice's and Bob's amplitude quadratures for the copropagation and counterpropagation of the classical lights and QKD. The wavelength of the QKD signal is 1539.37 nm. The other parameters are the same as those in Fig. 7.

($\upsilon_{B,\mathrm{el}} = 0.09$) and quantum efficiency $\eta_A = 86\%$ ($\eta_B = 55\%$), and the reconciliation efficiency of $\beta = 0.95$. Based on the experimental parameters, the channel excess noise estimates are 0.015 (10 km), 0.027 (20 km), 0.041 (30 km), 0.048 (40 km), and 0.07 (50 km), respectively, which are lower than the maximal tolerable channel noises of our entanglement-based CV QKD system with values 0.341 (10 km), 0.283 (20 km), 0.241 (30 km), 0.209 (40 km), and 0.184 (50 km). Therefore, we could generate secret keys in the classical data and quantum signal multiplexing channel.

In an actual optical communication system, each data channel is modulated independently and the resulting pulse modulation sequences of the channels are certainly different. In our experiment, five classical data channels are simultaneously modulated by one modulator for simplicity. The corresponding excess noise under the condition of independent pulse modulation sequences can be derived from Eqs. (32), (33), and (34). More precisely, the inferred excess noises of the degenerate and nondegenerate FWMs are determined to be 3/4 and 7/16 times the measured value in Fig. 7, respectively. On the other hand, the polarization directions of all the classical lights are aligned to be identical in our experiment to simulate the worst case, which results in an overestimation of the FWM efficiency by around 2 times if the classical channels have 50% overlap in their polarization states [32]. However, even if considering the abovementioned effects, the FWM-induced excess noises are still the dominant noise sources in the case of a relatively short optical fiber and quantum signal adjacent to the classical channels with narrow channel spacing.

V. CONCLUSION

For DWDM of strong classical data channels and CV QKD with narrow channel spacing over a single-mode fiber, FWM can be the dominant excess noise source when the optical fiber is relatively short and the quantum signal is adjacent to the classical channels. We establish a model to characterize the excess noise induced by FWM, and experimentally verify the validity of the theoretical predictions. The technique of unequal channel spacing is proposed to suppress the adverse effect of FWM on the CV QKD.

For copropagation of classical data channels and QKD, we find that the pulsed classical light can modulate the phase and amplitude of the carrier wave of the quantum signal, which degrade the correlation between Alice's and Bob's data and deteriorate the QKD performance. This XPM noise can be effectively avoided if the classical light and QKD are counterpropagating, which is confirmed in our experiment. In this scenario, we achieve the integration of the entangled state-based CV QKD and five adjacent DWDM classical channels with 10 dBm launch power and NRZ OOK modulation at 2.5 Gb/s (10 Gb/s).

In the future, to eliminate the XPM in the case of copropagation and enable a two-way transport of the classical channels, a two-mode squeezing vacuum state accompanied by a weak time and polarization multiplexed phase reference light can be employed. The distribution of continuous-variable entangled states over an optical fiber channel in which strong DWDM classical data channels are transported, not only enables the integration of classical communication and CV QKD with entangled states, but also paves the way for a future entanglement-based quantum communication network over an existing optical fiber network [33,34].

[1] N. Gisin, G. Ribordy, W. Tittel, and H. Zbinden, Quantum cryptography, Rev. Mod. Phys. **74**, 145 (2002).

[2] V. Scarani, H. B. Pasquinucci, N. J. Cerf, M. Dušek, N. Lütkenhaus, and M. Peev, The security of practical quantum key distribution, Rev. Mod. Phys. **81**, 1301 (2009).

[3] E. Diamanti, H. K. Lo, B. Qi, and Z. L. Yuan, Practical challenges in quantum key distribution, npj Quantum Inf. **2**, 16025 (2016).

[4] S. Pirandola, U. L. Andersen, L. Banchi, M. Berta, D. Bunandar, R. Colbeck, D. Englund, T. Gehring, C. Lupo, C. Ottaviani, *et al.*, Advances in quantum cryptography, arXiv:1906.01645.

[5] F. H. Xu, X. F. Ma, Q. Zhang, H. K. Lo, and J. W. Pan, Secure quantum key distribution with realistic devices, arXiv:1903.09051.

[6] P. D. Townsend, Simultaneous quantum cryptographic key distribution and conventional data transmission over installed fibre using wavelength-division multiplexing, Electron. Lett. **33**, 188 (1997).

[7] N. I. Nweke, P. Toliver, R. J. Runser, S. R. McNown, J. B. Khurgin, T. E. Chapuran, M. S. Goodman, R. J. Hughes, C. G. Peterson, K. McCabe *et al.*, Experimental characterization of the separation between wavelength-multiplexed quantum and classical communication channels, Appl. Phys. Lett. **87**, 174103 (2005).

[8] T. E. Chapuran, P. Toliver, N. A. Peters, J. Jackel, M. S. Goodman, R. J. Runser, S. R. McNown, N. Dallmann, R. J. Hughes, K. P. McCabe, *et al.*, Optical networking for quantum key distribution and quantum communications, New J. Phys. **11**, 105001 (2009).

[9] I. Choi, R. J. Young, and P. D. Townsend, Quantum information to the home, New J. Phys. **13**, 063039 (2011).

[10] L. J. Wang, K. H. Zou, W. Sun, Y. Q. Mao, Y. X. Zhu, H. L. Yin, Q. Chen, Y. Zhao, F. Zhang, T. Y. Chen, and J. W. Pan, Long-distance copropagation of quantum key distribution and terabit classical optical data channels, Phys. Rev. A **95,** 012301 (2017).

[11] Y. Q. Mao, B. X. Wang, C. X. Zhao, G. Q. Wang, R. C. Wang, H. H. Wang, F. Zhou, J. M. Nie, Q. Chen, Y. Zhao *et al.*, Integrating quantum key distribution with classical communications in backbone fiber network, Opt. Express **26,** 6010 (2018).

[12] J. F. Dynes, W. W.-S. Tam, A. Plews, B. Fröhlich, A. W. Sharpe, M. Lucamarini, Z. L. Yuan, C. Radig, A. Straw, T. Edwards, and A. J. Shields, Ultra-high bandwidth quantum secured data transmission, Sci. Rep. **6,** 35149 (2016).

[13] P. Eraerds, N. Walenta, M. Legré, N. Gisin, and H. Zbinden, Quantum key distribution and 1 Gbps data encryption over a single fibre, New J. Phys. **12,** 063027 (2010).

[14] K. A. Patel, J. F. Dynes, I. Choi, A. W. Sharpe, A. R. Dixon, Z. L. Yuan, R. V. Penty, and A. J. Shields, Coexistence of High-Bit-Rate Quantum Key Distribution and Data on Optical Fiber, Phys. Rev. X **2,** 041010 (2012).

[15] J. Mora, W. Amaya, A. R. Alba, A. Martinez, D. Calvo, V. G. Muñoz, and J. Capmany, Simultaneous transmission of 20 × 2 WDM/SCM-QKD and 4 bidirectional classical channels over a PON, Opt. Express **20,** 16358 (2012).

[16] N. A. Peters, P. Toliver, T. E. Chapuran, R. J. Runser, S. R. McNown, C. G. Peterson, D. Rosenberg, N. Dallmann, R. J. Hughes, K. P. McCabe *et al.*, Dense wavelength multiplexing of 1550 nm QKD with strong classical channels in reconfigurable networking environments, New J. Phys. **11,** 045012 (2009).

[17] K. A. Patel, J. F. Dynes, M. Lucamarini, I. Choi, A. W. Sharpe, Z. L. Yuan, R. V. Penty, and A. J. Shields, Quantum key distribution for 10 Gb/s dense wavelength division multiplexing networks, Appl. Phys. Lett. **104,** 051123 (2014).

[18] L. J. Wang, L. K. Chen, L. Ju, M. L. Xu, Y. Zhao, K. Chen, Z. B. Chen, T. Y. Chen, and J. W. Pan, Experimental multiplexing of quantum key distribution with classical optical communication, Appl. Phys. Lett. **106,** 081108 (2015).

[19] E. Diamanti and A. Leverrier, Distributing secret keys with quantum continuous variables: Principle, security and implementations, Entropy **17,** 6072 (2015).

[20] B. Qi, W. Zhu, L. Qian, and H. K. Lo, Feasibility of quantum key distribution through a dense wavelength division multiplexing network, New J. Phys. **12,** 103042 (2010).

[21] R. Kumar, H. Qin, and R. Alléaume, Coexistence of continuous variable QKD with intense DWDM classical channels, New J. Phys. **17,** 043027 (2015).

[22] D. Huang, D. K. Lin, C. Wang, W. Q. Liu, S. H. Fang, J. Y. Peng, P. Huang, and G. H. Zeng, Continuous-variable quantum key distribution with 1 Mbps secure key rate, Opt. Express **23,** 17511 (2015).

[23] F. Karinou, H. H. Brunner, C.-H. F. Fung, L. C. Comandar, S. Bettelli, D. Hillerkuss, M. Kuschnerov, S. Mikroulis, D. Wang, C. Xie *et al.*, Toward the integration of CV quantum key distribution in deployed optical networks, IEEE Photon. Technol. Lett. **30,** 650 (2018).

[24] T. A. Eriksson, T. Hirano, B. J. Puttnam, G. Rademacher, R. S. Luís, M. Fujiwara, R. Namiki, Y. Awaji, M. Takeoka, N. Wada, and M. Sasaki, Wavelength division multiplexing of continuous variable quantum key distribution and 18.3 Tbit/s data channels, Commun. Phys. **2,** 9 (2019).

[25] S. Kleis, J. Steinmayer, R. H. Derksen, and C. G. Schaeffer, Experimental investigation of heterodyne quantum key distribution in the S-band or L-band embedded in a commercial C-band DWDM system, Opt. Express **27,** 16540 (2019).

[26] T. F. da Silva, G. B. Xavier, G. P. Temporão, and J. P. von der Weid, Impact of Raman scattered noise from multiple telecom channels on fiber-optic quantum key distribution systems, IEEE J. Lightwave Technol. **32,** 2332 (2014).

[27] J. N. Niu, Y. M. Sun, C. Cai, and Y. F. Ji, Optimized channel allocation scheme for jointly reducing four-wave mixing and raman scattering in the DWDM-QKD system, Appl. Opt. **57,** 7987 (2018).

[28] T. A. Eriksson, T. Hirano, M. Ono, M. Fujiwara, R. Namiki, K. I. Yoshino, A. Tajima, M. Takeoka, and M. Sasaki, Coexistence of continuous variable quantum key distribution and 7 × 12.5 Gbit/s classical channels, IEEE Summer Topical Meeting Series (SUM) (2018).

[29] Q. Lin, F. Yaman, and G. P. Agrawal, Photon-pair generation in optical fibers through four-wave mixing: Role of Raman scattering and pump polarization, Phys. Rev. A **75,** 023803 (2007).

[30] R. W. Tkach, A. R. Chraplyvy, F. Forghieri, A. H. Gnauck, and R. M. Derosier, Four-photon mixing and high-speed WDM systems, IEEE J. Lightwave Technol. **13,** 841 (1995).

[31] N. Wang, S. N. Du, W. Y. Liu, X. Y. Wang, Y. M. Li, and K. C. Peng, Long-Distance Continuous-Variable Quantum Key Distribution with Entangled States, Phys. Rev. Appl. **10,** 064028 (2018).

[32] K. Inoue, Polarization effect on four-wave mixing efficiency in a single-mode fiber, IEEE J. Quantum Electron. **28,** 883 (1992).

[33] H. J. Kimble, The quantum internet, Nature **453,** 1023 (2008).

[34] S. Wengerowsky, S. K. Joshi, F. Steinlechner, H. Hübe, and R. Ursin, An entanglement-based wavelength-multiplexed quantum communication network, Nature **564,** 225 (2018).